Materials Today Bio 29 (2024) 101257

Contents lists available at ScienceDirect

Materials Today Bio

journal homepage: www.journals.elsevier.com/materials-today-bio

Data encryption/decryption and medical image reconstruction based on a sustainable biomemristor designed logic gate circuit

Fulai Lin [a,b], Yuchen Cheng [d], Zhuoqun Li [a,e], Chengjiang Wang [a,b], Wei Peng [a,b], Zelin Cao [c], Kaikai Gao [c], Yu Cui [c], Shiyang Wang [a], Qiang Lu [a], Kun Zhu [f], Dinghui Dong [a,e], Yi Lyu [a,b,e], Bai Sun [a,c,*], Fenggang Ren [a,e,**]

[a] National Local Joint Engineering Research Center for Precision Surgery and Regenerative Medicine, The First Affiliated Hospital of Xi'an Jiaotong University, Xi'an, Shaanxi, 710061, China
[b] School of Future Technology, Xi'an Jiaotong University, Xi'an, Shaanxi, 710049, China
[c] Frontier Institute of Science and Technology (FIST), Xi'an Jiaotong University, Xi'an, Shaanxi, 710049, China
[d] State Key Laboratory of Electrical Insulation and Power Equipment, Xi'an Jiaotong University, Xi'an, 710049, China
[e] Department of Hepatobiliary Surgery, The First Affiliated Hospital of Xi'an Jiaotong University, Xi'an, Shaanxi, 710061, China
[f] Department of Neurology, The First Affiliated Hospital of Xi'an Jiaotong University, Xi'an, Shaanxi, 710061, China

ARTICLE INFO

Keywords:
Biomemristor
Biomaterials
Multifunctional device
Logic gate circuits
Medical image
Data encryption

ABSTRACT

Memristors are considered one of the most promising new-generation memory technologies due to their high integration density, fast read/write speeds, and ultra-low power consumption. Natural biomaterials have attracted interest in integrated circuits and electronics because of their environmental friendliness, sustainability, low cost, and excellent biocompatibility. In this study, a sustainable biomemristor with Ag/mugwort:PVDF/ITO structure was prepared using spin-coating and magnetron sputtering methods, which exhibited excellent durability, significant resistance switching (RS) behavior and unidirectional conduction properties when three metals were used as top electrode. By studying the conductivity mechanism of the device, a charge conduction model was established by the combination of F-N tunneling, redox, and complexation reaction. Finally, the novel logic gate circuits were constructed using the as-prepared memristor, and further memristor based encryption circuit using 3-8 decoder was innovatively designed, which can realize uniform rule encryption and decryption of medical information for data and medical images. Therefore, this work realizes the integration of memristor with traditional electronic technology and expands the applications of sustainable biomemristors in digital circuits, data encryption, and medical image security.

1. Introduction

With the rapid development of technology, traditional circuit integration and in-memory computing are subject to the dual limitations of Moore's law and von Neumann architecture, especially in terms of energy consumption, read/write speed, integration density, and flexibility [1,2]. Moreover, the exponential growth of various types of data in the information age has led to an increasingly widespread application of data encryption and image reconstruction technologies [3–5]. Therefore, integrated computation and memory technologies have emerged as a research hotspot. Memristor, an emerging nonvolatile memory and computation integration technology, shows great potential applications in various fields [6]. Memristor facilitate high-density integration, which makes them ideal for high-performance computing and memory systems [7]. Additionally, memristors are excellent for simulating synaptic functions similar to the human brain, providing new ways to develop artificial intelligence and neural networks [7–9]. The primary feature of a memristor is its resistance switching (RS) characteristic with hysteresis current–voltage (*I*–*V*) curve. Specifically, its resistance state can be reversibly switched between high–resistance state (HRS) and

* Corresponding author. National Local Joint Engineering Research Center for Precision Surgery and Regenerative Medicine, The First Affiliated Hospital of Xi'an Jiaotong University, Xi'an, Shaanxi, 710061, China.
** Corresponding author. National Local Joint Engineering Research Center for Precision Surgery and Regenerative Medicine, The First Affiliated Hospital of Xi'an Jiaotong University, Xi'an, Shaanxi, 710061, China.
E-mail addresses: baisun@xjtu.edu.cn (B. Sun), renfenggang@xjtu.edu.cn (F. Ren).

https://doi.org/10.1016/j.mtbio.2024.101257
Received 2 August 2024; Received in revised form 13 September 2024; Accepted 17 September 2024
Available online 17 September 2024

low–resistance state (LRS) based on the direction and magnitude of the applied voltage [10]. The RS behavior of the memristor is usually determined by the charge flowing through the functional layer, implying that the RS characteristic can be adjusted by controlling the charge flow within functional layer of the memristor [11,12]. Therefore, memristor is one of the most promising new electronic devices that can overcome the limitations of traditional technology.

Memristors can perform logic operations based on two variables, which are used in logic gates and latches, using resistance instead of voltage or charge as the physical variables [13,14]. Besides, memristors can also implement Boolean logic gates based on temporal order and are characterized by fast operation and low power consumption [15]. Kuma et al. implemented an extreme learning machine algorithm using a combination of memristor crossbar array and complementary metal–-oxide semiconductor (CMOS) circuits, and designed an encoder unit for classification tasks on real-time datasets [16]. Secure and efficient transmission and storage of sensitive medical information have become important challenges, especially for medical images with huge data volume, high redundancy and strong correlation [17]. Compared to traditional encryption techniques based on software algorithms alone, memristor based encryption reduces energy consumption and increases the speed of encryption and decryption processes [18,19]. Lin et al. developed a memristive-coupled neural network model for biomedical image encryption based on two neural networks and one memristor synapse [20]. Furthermore, Yang et al. designed a chaotic system based on the Chebyshev chaotic system and a memristor model to encrypt three-dimensional medical images, which can resist typical encryption attacks [21]. However, in practical applications, it is important to prioritize simplicity of operation for the user (patient and physician) and effectiveness of encryption [22]. Therefore, it is necessary to develop an efficient hardware-encryption method based on memristors with low power consumption and high integration density, which can provide technical support for ensuring the security of medical data in the era of big data.

The performance of memristors mainly depends on the functional layer and electrode materials used to construct the core structure of the device [23]. A memristor is a three-layer structure, where metals or conductive oxides are typically used as the top and bottom electrodes [24–26]. Various materials are available for the functional layers of memristors, including metal oxides, ferroelectric materials, organic materials, and two-dimensional materials [27–29]. Among these, metal oxides as functional layer are extensively studied due to their excellent stability and durability [28–30]. However, memristors based on metal oxides still have some limitations, such as environmental pollution and poor biocompatibility [31]. The use of biomaterials as functional layer materials in devices can significantly reduce the release of toxic substances during the production and disposal process of electronic devices [32]. Additionally, biomaterials are often readily available from abundant sources and are inexpensive. Hota et al. prepared a biomemristor with a high dynamic response using natural silk fibroin protein of silkworm [33]. Han et al. prepared an Ag/Au-fibril hybrid/Pt structured memristor and demonstrated the potential applications as biocompatible device [34]. Chen et al. investigated a highly durable and biocompatible memristor, demonstrating its broad application as the next generation of implantable multi–resistor memories for health detection [6]. Therefore, these studies proved the potential of biomemristors in realizing multiple functions such as hardware-circuit encryption.

In this work, an Ag/mugwort:PVDF/ITO structured biomemristor with excellent RS behavior and unidirectional conduction properties was prepared. By fitting the *I-V* curves of the device in logarithmic form, the mechanism was attributed to a charge conduction mode driven by the combination of Fowler–Nordheim (F–N) tunneling, oxidation reaction and complexation reaction. Finally, the as-prepared memristors were used to fabricate novel logic circuits, and the decoder-based encryption circuits were devised to enable encryption and decryption of ASCII code data and medical image. This work enables the combination of memristors with conventional electronic devices and expands the applications of memristors in digital circuits and data security encryption. These results advance the new research fields of biomemristor applications and medical information security.

2. Experimental section

2.1. Materials and reagents

In the same harvest period, mugwort leaves were harvested from Bozhou, Anhui Province, China. First, the mugwort leaves were rinsed with deionized water four times and dried naturally. Subsequently, the dried mugwort leaves were processed by mechanical grinding and ball milling (QM-2SP20, Xinnuo Instrument Co., Ltd., Shanghai, China) to prepare mugwort powder. Ball milling was conducted at a power of 50 W and running time of 120 min. Unless otherwise stated, the reagents used in this experiment, such as N-methylpyrrolidone (NMP) and polyvinylidene difluoride (PVDF), were purchased from Macklin Biochemical Co., Ltd., Shanghai, China.

2.2. Devices fabrication

The memristors were prepared by spin-coating and magnetron sputtering. First, the ITO substrates with an area of 2 × 2 cm were ultrasonically cleaned for 15 min with deionized water, anhydrous ethanol and deionized water, respectively. Then, ITO substrates were cleaned with a plasma cleaner for 10 min. Mugwort powder (1 g) was mixed with NMP (2.5 mL) at 60 °C under constant-temperature magnetic stirring for 120 min. The supernatant was obtained by separating the completely dissolved solution from the solid and liquid. The supernatant was then mixed with PVDF to obtain a solution. The as-obtained solution was applied to the ITO-coated glass substrate via spin-coating method, with the spin-coater set to 200 rpm for 10 s and then 1000 rpm for 15 s. The mugwort:PVDF film was then dried at 60 °C for 24 h to remove volatile components. Finally, the device fabrication was completed by depositing the Ag as the top electrode via magnetic sputtering using a metal mask. In addition, memristors with Cu/mugwort:PVDF/ITO structures and Ti/mugwort:PVDF/ITO structures follow the same manufacturing process described above.

2.3. Characterization and circuit simulation

The surface micro-morphology of the memristor and the cross-sectional thickness of the sample were characterized by scanning electron microscopy (SEM, Zeiss, Sigma300, Germany). The structural information and elemental composition of the mugwort:PVDF films were determined by X-ray diffraction (XRD, Rigaku Ultima IV, Japan) and X-ray photoelectron spectroscopy (XPS, ESCALAB 250Xi+, America). The energy bandwidths were investigated using Ultraviolet photoelectron spectroscopy (UPS, Thermo Scientific, ESCALAB Xi+, America) and Ultraviolet–Visible (UV–vis) spectroscopy (Hitachi, UH4150, Japan). The *I–V* curves of the device were measured by the electrochemical workstation equipped with a source meter (B2900, Keysight, Beijing, China) and a probe station (XIBI Semiconductor Technology Co., Ltd, Shanghai, China). The memristor-based circuit simulations were conducted using the Simulink module of MATLAB (MathWorks, R2022b, USA).

3. Results and discussion

3.1. Microscopic characterization of memristor

The biomemristor was prepared using spin-coating and magnetron sputtering methods (Fig. 1a) [35,36]. Mugwort leaves were cleaned, dried, and then mechanically ground into superfine powder. After mugwort powder was mixed with NMP and PVDF to create a solution,

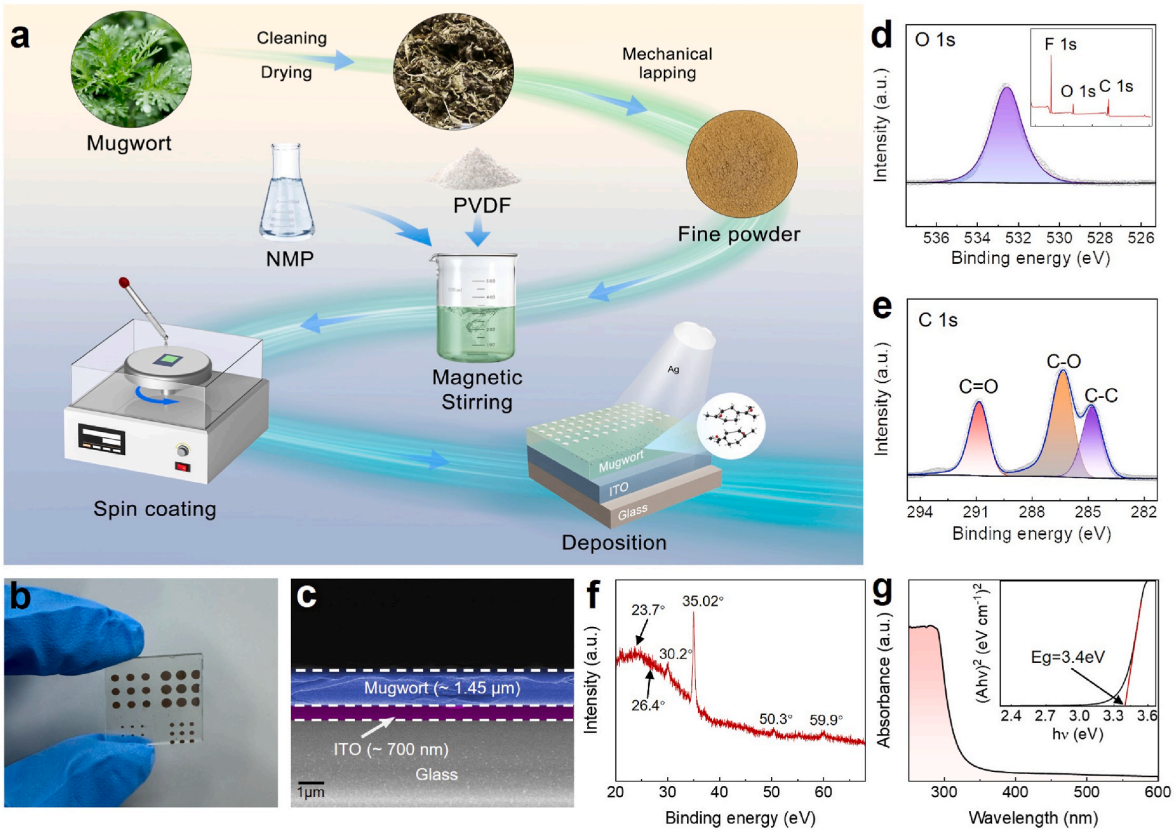

Fig. 1. (a) Schematic of the biomemristor fabrication process. (b) Photograph of the as-prepared memristor. (c) Cross-sectional SEM morphology of the device. (d, e) XPS test of the as-prepared memristor. (f) XRD test of the mugwort:PVDF film. (g) UV–vis spectrum and corresponding Tauc plot (inset) of the mugwort:PVDF film.

the solution was then spin-coated onto an ITO substrate. The substrate was covered with a mask, and then Ag was sputtered onto the surface of the mugwort: PVDF to serve as the top electrode of the device. Finally, the Ag/mugwort:PVDF/ITO memristor was subjected to *I-V* testing (Fig. S1). The structure of the as-fabricated memristor is shown in Fig. 1b and c, from which it can be seen that the ITO thickness is approximately 700 nm and the thickness of mugwort:PVDF film is approximately 1.45 μm. To evaluate the composition and structure of the as-fabricated mugwort:PVDF film, the film was subjected to XPS testing (Fig. 1d and e). The major elements of the mugwort: PVDF film were F, C, and O (the F element was from PVDF), which was also confirmed by the XRD testing (Fig. 1f). The intrinsic band gap of mugwort:PVDF is 3.4 eV by using UV–vis spectra and the corresponding Tauc plot (Fig. 1g). As a result, an Ag/mugwort:PVDF/ITO structured memristor was prepared without impurities.

3.2. *Effect of top electrode on biomemristor*

The performance of memristive devices is significantly affected by different electrode materials due to their different metal activities, binding energies, and valences [37–39]. To investigate the effect of different electrodes on the performance of the biomemristor, Cu, Ti, and Ag were used as the top electrode materials (Fig. 2**)**. Each memristor with a different top electrode was scanned for 100 cycles by applying bias voltage sequence. Among them, the Cu/mugwort:PVDF/ITO structured memristor showed insignificant RS behavior and the *I-V* curve of the memristor gradually lost the curve window with the increasing number of scanning cycles, which indicated the poor stability of the Cu as top electrode based memristor (Fig. 2a). Subsequently, the memristor with Ti/mugwort:PVDF/ITO structure has a significant RS behavior and the window of the *I-V* curve gradually stabilized as the increasing of scanning cycles number (Fig. 2b). Notably, the resistance state of the memristor was changed from LRS to HRS when the bias voltage was increased, which was contrary to the case of the memristor with Cu as the top electrode. This may occur due to C atom related reactions in the biomaterials used as the functional layer, as demonstrated by Park et al., who fabricated the Au/lignin/ITO/flexible memristor with polyethylene terephthalate substrate [40].

When the top electrode material was changed to Ag, the memristor with the Ag/mugwort:PVDF/ITO structure exhibited excellent RS behavior and unidirectional conductivity. Specifically, the resistance state of the memristor can be switched from HRS to LRS when a positive bias voltage was applied, and remained at HRS when a negative bias voltage was applied. Additionally, the *I-V* curve window of the memristor with Ag as the top electrode remained stable even after 100 scanning cycles, indicating excellent stability. Fig. 2d–f displays the *I-V* curves of three different memristors on a semi-logarithmic scale. The Ag/mugwort:PVDF/ITO structured device exhibits excellent RS performance and stability. The HRS and LRS of a memristor are crucial parameters for determining memristor characteristics, and a higher HRS/LRS ratio represents excellent RS behavior and a low misreading rate [41,42]. To compare the effect of three top electrodes on the HRS/LRS resistance ratio, the HRS and LRS of the devices were tested at specific voltages (1.0, 2.5, and 0.4 V). The test voltages were chosen to correspond to the maximums of the windows of the *I-V* curves (Fig. 2g–i). The HRS/LRS resistance ratio of the memristor with Cu as the top electrode is the lowest (~1.05), and the resistance at HRS is unstable in the first 20 cycles. Therefore, the memristor with Ag as the top electrode has the best RS performance with the resistance ratio of approximately 3.6 and stability. To investigate the optimal operating conditions and potential application of the Ag/mugwort:PVDF/ITO structured memristor, its RS behavior was analyzed at various bias voltages and scan rates.

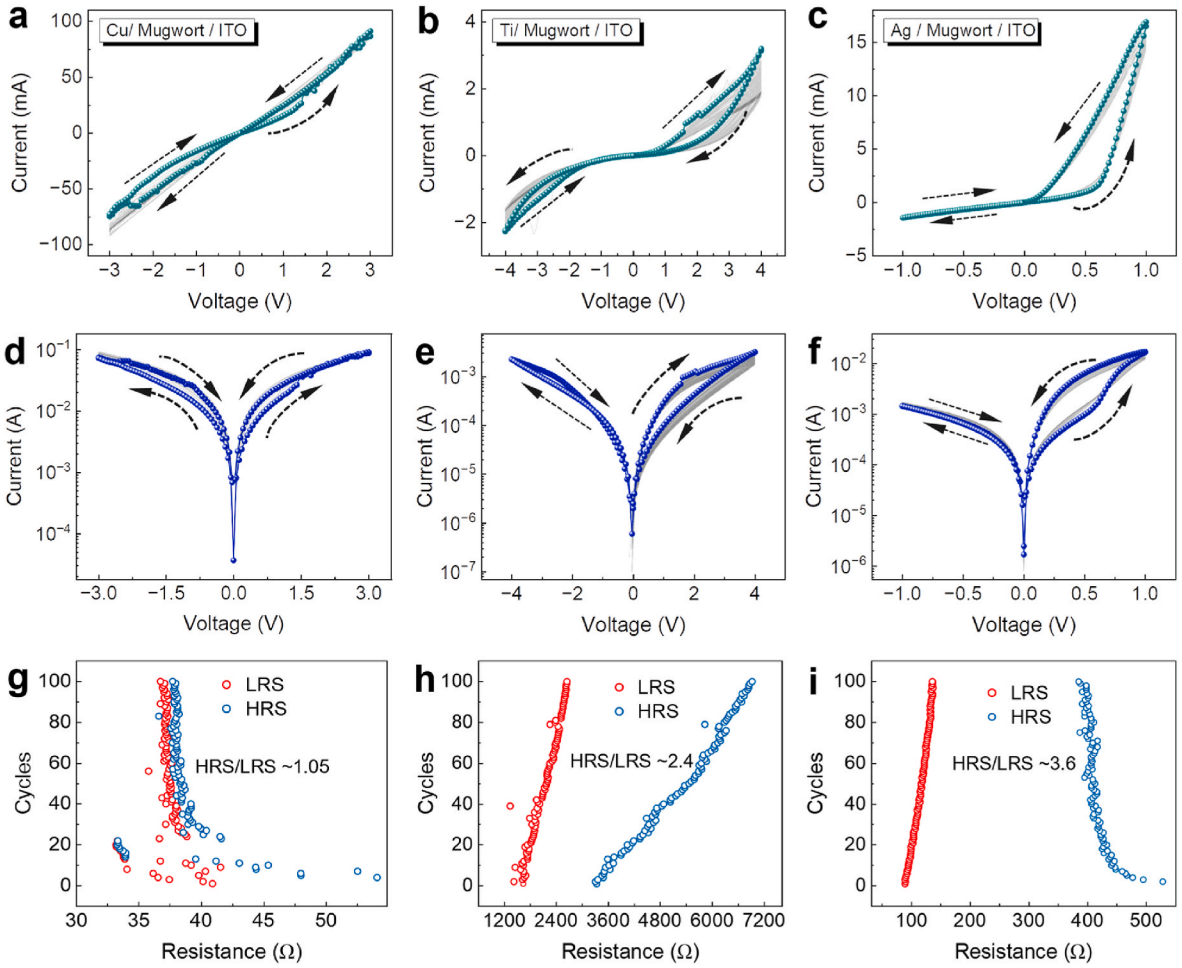

Fig. 2. (a) *I–V* characteristic curves of the device when Cu was used as the top electrode. (b) Ti as top electrode. (c) Ag as top electrode. (d, e, f) Semilogarithmic *I–V* characteristic curves of the devices. (g, h, i) Corresponding resistance value of the device at the HRS and LRS and the HRS/LRS resistance ratio.

3.3. Unidirectional conduction property of the biomemristor

Fig. 3a shows the *I-V* curves of the Ag/mugwort:PVDF/ITO memristor under different voltage amplitudes (±0.5 V, ±1.0 V, ±1.5 V, and ±2.0 V). The *I-V* curves show that the SET voltage of the device is increased with the voltage amplitude, suggesting that the threshold voltage of the memristor could be affected by the voltage amplitude, similar to the results of a previous study (Fig. S2) [43]. The unidirectional conduction property of the memristor is disappeared when the voltage amplitude is less than ±0.8 V or more than ±1.5 V. This can be ascribed to the too small voltage to reach the SET voltage or increased conductivity of the functional layer owing to the increase of the number of Ag^+ ions in the functional layer under high voltage [44,45]. The HRS and LRS of the memristor first increases and then decreases, and the HRS/LRS ratio reaches the maximum value at 1.0 V, which is about 3.6 (Fig. 3c). To investigate the effects of scanning rate on the RS behavior and unidirectional conduction property of the memristor, Fig. 3b shows the *I-V* curves measured at the voltage amplitude of ±1.0 V and various voltage scanning rates (0.5, 1.0, 1.4, and 2.0 Vs^{-1}). The resistance window of the memristor is reached its largest value when the voltage scanning rate is 1.0 Vs^{-1} (Fig. S3). The LRS of the memristor remained relatively constant with the voltage scan rate was increased from 0.5 Vs^{-1} to 3.0 V s^{-1}, while the HRS initially decreases and then gradually increased (Fig. 3d). The reason for this phenomenon is that the injected electrons could undergo the trapping/de-trapping process when the scan rate was less than 2.0 Vs^{-1}, but they lacked sufficient time to complete the process at higher voltage scan rates [46,47].

Fig. 3e shows the *I-V* curves of the diode and the Ag/mugwort:PVDF/ITO memristor. The diode exhibits excellent unidirectional conduction properties (diode conducts at forward voltage and cuts off at reverse voltage). This implies that the diode current surge significantly when the forward voltage surpasses the conduction voltage (V_{on}), whereas the current remains low at the reverse voltage. Diode breakdown becomes a risk if the reverse voltage exceeds the breakdown voltage (V_{BRS}). The memristor exhibits comparable unidirectional conduction property, specifically the current in the memristor rapidly increases when the voltage amplitude is higher than V_{set} in the positive voltage region (PVR), whereas it remains low in the negative voltage region (NVR). Forward and reverse current and their ratio (F/R Ratio) are crucial indicators of unidirectional conduction (Fig. 3f) [48]. The F/R Ratio was measured at different voltage amplitudes and scanning rates, and the results indicated that unidirectional conduction property was best at a voltage amplitude of ±1.0 V and a scan rate of 1.0 Vs^{-1} (Fig. 3h). Under these parameters, the forward and reverse current and F/R Ratio corresponding to each equal voltage of the memristor were tested, and the results showed that the F/R Ratio reached the maximum value (~12) at approximately 0.9 V (Fig. 3g).

3.4. Mechanism of biomemristor

The physical phenomena of both RS behavior and unidirectional conduction characteristics are rare in memristors, so it is necessary to further analyze the working mechanism in this study. The *I-V* curve in the PVR was segmented into three parts for analysis: the HRS (step 1),

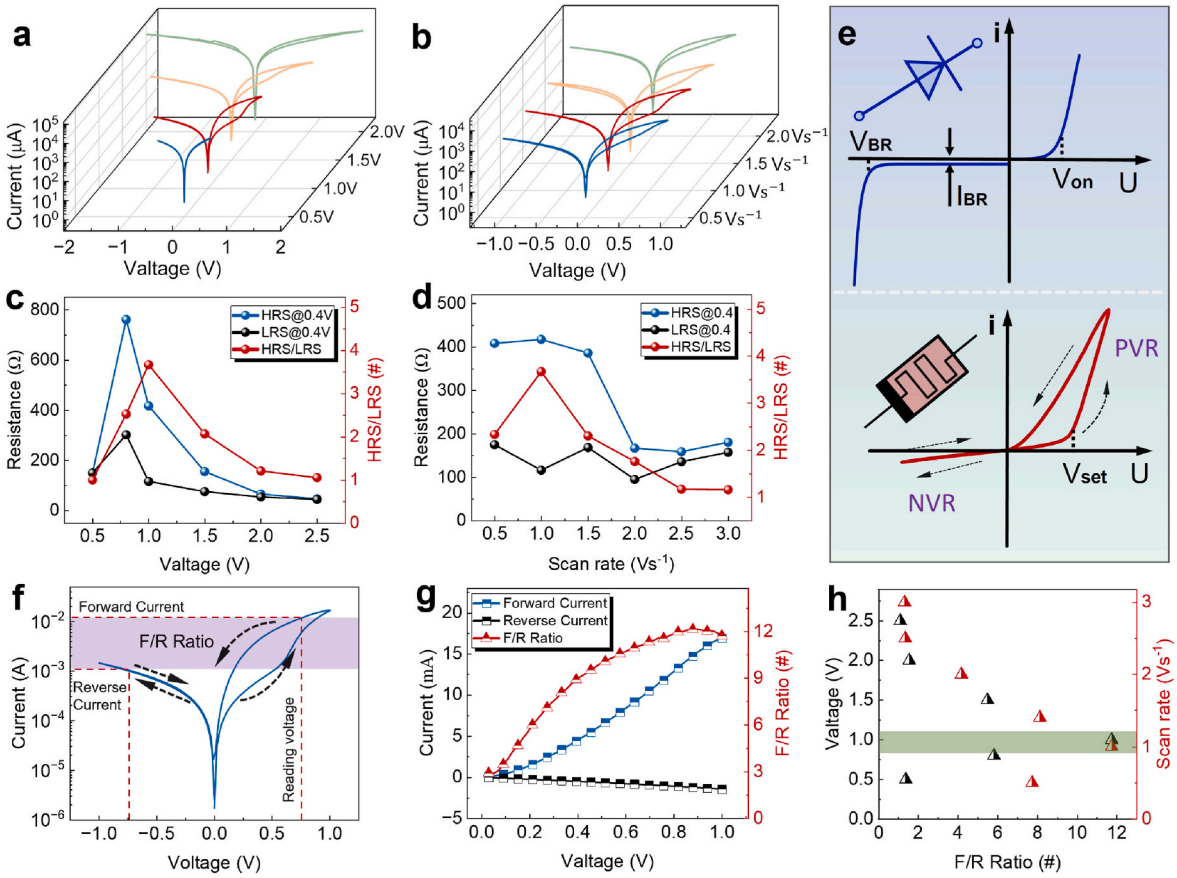

Fig. 3. I–V curves of the Ag/mugwort:PVDF/ITO memristor under (a) different voltages and (b) different scanning rates. Comparison of the HRS and LRS of the Ag/mugwort:PVDF/ITO memristor under (c) different voltages and (d) different scanning rates. (e) *I-V* curves of the diode and the memristor. (f) Measurement of the F/R Radio. (g) Variation of F/R Radio vs reading voltages under the voltage amplitude of ±1.0 V. (h) Effect of different voltage amplitudes and scanning rates on the F/R Radio of the device.

the high voltage region of the LRS (step 2), and the low voltage region of the LRS (step 3) (Fig. 4a) [48]. In step 1, the characteristic curve of the memristor in the voltage range of 0.48–1.0 V was analyzed using the F-N tunneling model [49,50]:

$$I \propto V^2 \exp\left(-\frac{4d\sqrt{2m^*\Phi_n{}^3}}{3hqV}\right) \tag{1}$$

where q is the charge, d is the barrier width, m^* is the effective mass of the electron, ϕ_n is the barrier height, and h is Planck's constant. The equation can also be simplified as:

$$Ln\left(\frac{I}{V^2}\right) \propto -\frac{1}{V} \tag{2}$$

The slope of the curve is −1.5 when V^{-1} increased from 0 to 2.04, and it abruptly changed to a positive value when V^{-1} exceeded 2.04 (~0.49 V). The shape of the interfacial barrier gradually changed from trapezoidal to triangular with increasing bias voltage, indicating that the charge transport mechanism can be switched from direct tunneling to F-N tunneling with increasing applied voltage.

In step 2, the Schottky conduction model is fitted to the high voltage region from 1.0 V to 0.49 V, and the slope is 3.38. The fitting result indicates that the charge conduction behavior is consistent with Schottky conduction, indicating that some of the electrons are trapped during the conduction process (Fig. 4c) [51,52]. The Schottky conduction model and its simplified form can be described separately as [53]:

$$J = \frac{4\pi q m^* (kT)^2}{h^3} \exp\left[\frac{q\left(\Phi_n - \sqrt{\frac{qV}{4\pi\varepsilon}}\right)}{kT}\right] \tag{3}$$

$$\mathrm{Ln}(I) \propto V^{1/2} \tag{4}$$

where J is the current density, T is the absolute temperature, k and ε are the Boltzmann and dielectric constants, respectively. Based on simplified Equation (4), Ln(J) and $V^{½}$ has a linear relationship, so the mechanism in this region could be explained by the Schottky conduction. The energy band structure of the memristor is depicted in Fig. 4f, illustrating that the valence band and band gap of mugwort:PVDF film are 4.9 and 3.4 eV, respectively.

In step 3, the charge transport mechanism is changed to direct tunneling, where the energy gained by the electrons decreases due to the reduction of the voltage (Fig. 4d). The *I-V* curves in the NVR were subjected to a double-logarithmic linear fit, which showed that the slope of the fit (~1.0) was consistent with the Ohmic conduction model (Fig. 4e) [44]. In summary, the mechanism of the memristor is influenced by a combination of factors, and the mechanism of Ag/mugwort:PVDF/ITO memristor cannot be fully explained by curve fitting alone. As a natural biomaterial, mugwort contains numerous chemical components, with the highest proportion being terpenes [54,55]. Considering the wide variety of terpenes, this work took limonene as an example to investigate the interaction between Ag^+ ions in the functional layer and their interfaces. Limonene typically exists in two

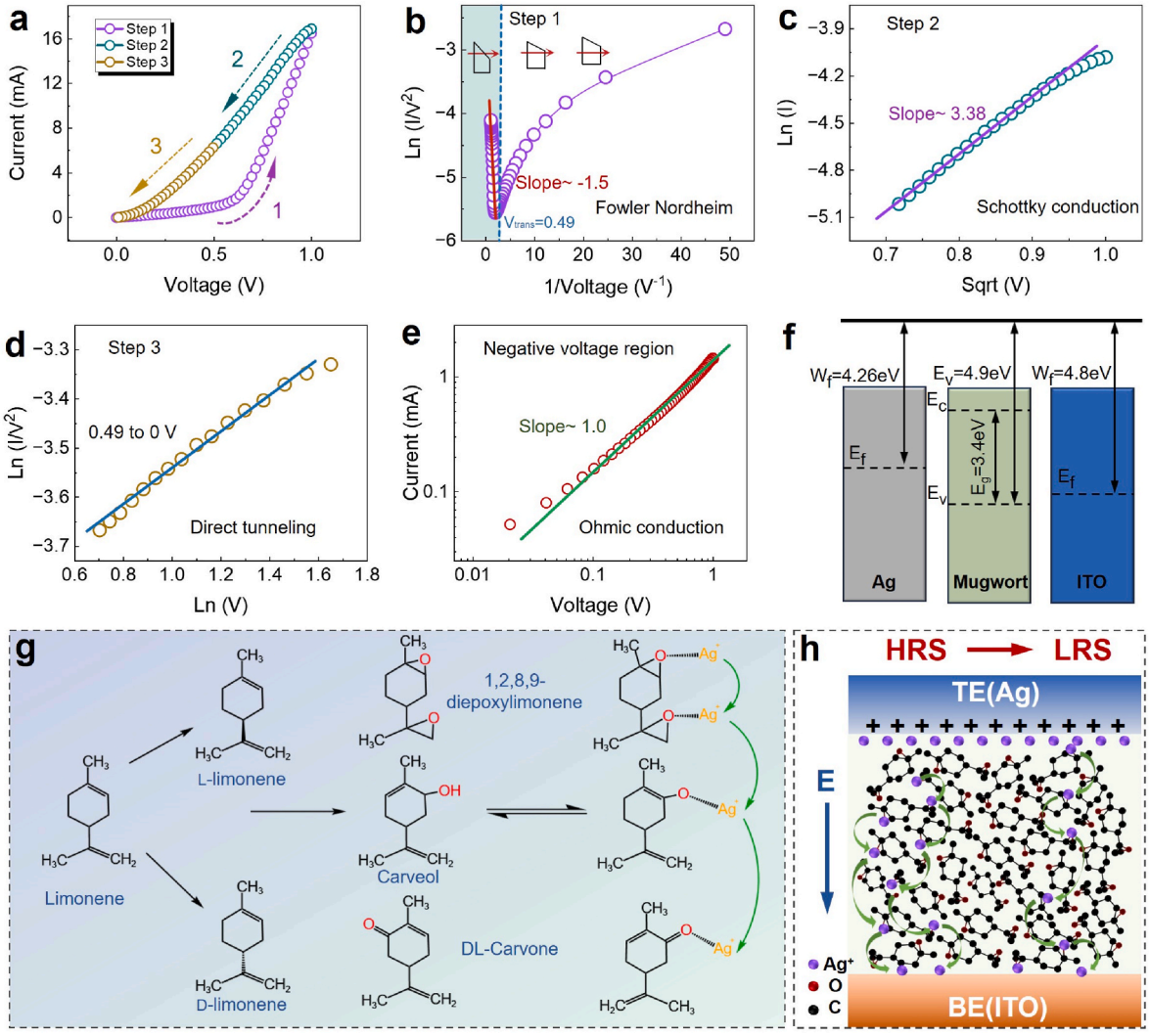

Fig. 4. (a) *I–V* curve of the device at 0 V → 1 V → 0 V. Fitting curves for the (b) F–N tunneling at 0 V → 1 V, (c) Schottky emission at 1.0 V → 0.49 V, (d) direct tunneling at 0.49 V → 0 V, and (e) ohmic conduction at 0 V → −1 V. (f) Band schematic of the Ag/mugwort:PVDF/ITO structure. (g) Mechanism of Ag^+ ions forming coordination complexes with limonene epoxides. (h) Schematic of the physical model of resistance state change.

isomers and is easily oxidized to form various limonene epoxides.

Fig. 4g illustrates three common oxides: 1,2,8,9-diepoxylimonene, carveol, and DL-carvone [56,57]. Initially, the application of an applied positive voltage to the top electrode resulted in the oxidation of Ag atoms, forming a small portion of Ag^+ ions at the interface. Concurrently, the functional groups in the functional layer were oxidized by the electric field to produce oxides such as DL-carvone. The memristor was in HRS owing to the low electric field energy acquired by the charge, along with direct tunneling. Upon the application of a bias voltage exceeding the threshold (0.49 V), Ag^+ ions were injected into the functional layer, causing the gradual triangularization of the interfacial barrier. This action induced energy band bending to induce the passage of electrons. As limonene oxides contained functional groups such as C-O-C and C-O-H, they could be interacted with metal ions such as Ag^+ to form coordination complexes [52,58]. The injected Ag^+ ions kept jumping towards the bottom electrode under the electric field, which were trapped by oxygen atoms on molecules such as carveol until reaching the bottom electrode [59]. The conductivity of the functional layer was increased, which caused the resistance state to switch from HRS to LRS (Fig. 4h). When the bias voltage was decreased from 1 V to 0 V, the coordination complex between Ag^+ ions and the organic oxide broke down, increasing the resistance of the memristor. When positive voltage was applied to the bottom electrode (ITO), the Ag^+ ions were moved towards the top electrode and were reduced to Ag atoms at the interface. And a part of the organic oxides underwent a reduction reaction, which caused the resistance of memristor to become HRS. In summary, a charge conduction model, which is driven by a combination of F-N tunneling, redox, and complexation reactions, is proposed to explain the mechanism of the Ag/mugwort:PVDF/ITOmemristor.

3.5. *Logic circuits based on biomemristors*

The memristor with Ag/mugwort:PVDF/ITO structure exhibites both RS behavior and unidirectional conduction properties. Unlike memristors with bipolar RS behavior, the memristor is more suitable for logic regulation because it does not need an additional reset threshold voltage, which increases applicability of the memristor in logic gates [13,60]. Given that CMOS devices currently represent the dominant logic gate circuit element, the integration of memristors with CMOS will drive the further application of memristors, which is also a challenge [61]. The resistance states during forward and reverse current flow are defined as LRS and HRS, respectively [35]. In this work, the Simulink module in MATLAB (MathWorks, R2022b, USA) was used to build and simulate logic circuits based on a biomemristor. Simulation parameters matched those of the memristor characteristics during simulation where HRS was 757Ω, LRS was 107Ω, high level input was 1.0V, and low level

input was 0.1V. The AND and OR logic gate circuits were built by connecting two memristors in series with each other in the opposite (or positive) direction (Fig. 5a–c). The histograms of the input and output voltages showed that the logic outputs of the circuit were well differentiated, where the output threshold was defined to be 0.6 V (Fig. 5b–d). The results demonstrated that the constructed logic gate circuits were in accordance with the logic truth tables of AND and OR (Fig. S4).

The three-input AND and OR logic gate circuits were successfully constructed, and the results showed that the output logic values were consistent with the truth table (Fig. S5). Subsequently, traditional CMOS devices were integrated into the circuit to further extend the functionality of the logic circuits based on memristors. Then, the CMOS NOT units were connected behind the AND and OR logic gate circuits to construct the NAND and NOR logic gates, where the value of V^+ was 1V (Fig. 5e–g). The simulation numerical results and the truth tables of the corresponding logic gates were compared to confirm the logic relationships (Fig. S4). The histograms generated from the simulation results showed that the NAND and NOR logic gates with CMOS NOT units were successfully constructed (Fig. 5f–h).

Furthermore, XOR logic gates were constructed by connecting the outputs of AND and OR logic gates consisting only of memristors to the inputs of the CMOS NOT units, respectively (Fig. 5j–k). The output result was "0″ when the levels of the two inputs were the same, and the output result of the XNOR logic gate circuit was the opposite, which was consistent with the truth table (Fig. S6). With these results, it was shown that the biomemristor with unidirectional conduction properties can not only be connected in series to realize logic judgments, but can also be integrated with CMOS devices to realize a variety of logic circuit applications. To test the potential of the memristor logic circuits for large-scale integration, a 3-8 decoder was constructed to employ a biomemristor. The 3-8 decoder was composed of eight three-input AND logic gates and three CMOS NOT units. The outputs of the 3-8 decoder based on biomemristors were compared with the truth table, and the results showed that the three inputs were logically correctly related to the eight outputs (Fig. S7). Then, the 0, 2, 3, and 7 output ports of the 3-8 decoder based on the biomemristors were connected into one output using two OR logic gates, and the remaining four output ports were connected in the same way. This novel circuit altered the one-to-one correspondence between the inputs and outputs of the 3-8 decoder into a many-to-one logical relationship, and it was defined as an encryption circuit based on biomemristor (Fig. 5i). The correspondence between the output value of the encryption circuit and the truth table is shown in Fig. S8, where the threshold voltage is changed to 0.3 V.

3.6. Encryption and decryption of medical information

With the development of medical digitization, medical data has shown exponential growth and its complexity has also significantly

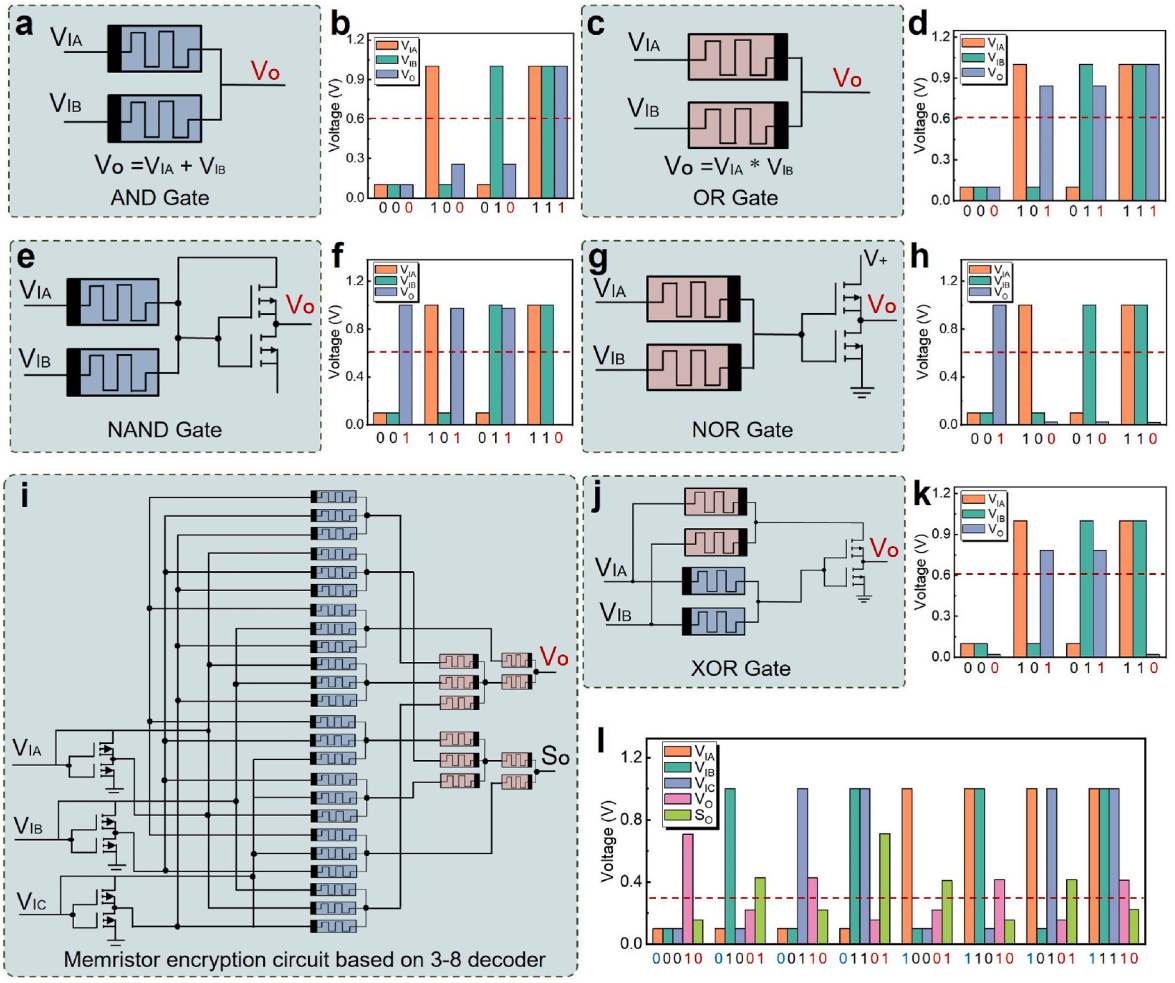

Fig. 5. (a) AND logic gate based on the biomemristor and (b) its simulation results. (c) OR logic gate based on the biomemristor and (d) its simulation results. (e) NAND logic gate based on the biomemristor and (f) its simulation results. (g) NOR logic gate based on the biomemristor and (h) its simulation results. (i) Memristor encryption circuit based on 3-8 decoder. (j) XOR logic gate based on biomemristor and (k) its simulation results. (l) Histogram of the simulation results of the encryption circuit.

increased [62]. Notably, medical imaging data is vast, and ensuring the secure and efficient storage of such large sensitive medical data is a major challenge in the medical field [63]. In this study, an encryption unit based on the established 3-8 decoder memristor circuit was constructed (Fig. 6a). The input X of the encryption unit correspond to the original data for encryption, whereas inputs Y and Z correspond to two keys (Fig. 6b). Subsequently, m × n encryption units were integrated into a hardware-based encryption circuit for encryption and decryption (Fig. 6c). It is well known that characters and numbers can be encoded using ASCII rules, where each symbol is linked to an 8-bit binary array. For instance, "D" can be encoded as "01000100", with "1" denoting a high level and "0" representing a low level. "D r e a m" was encrypted by the memristor encryption circuit based on 3-8 decoder into "9 % i Z s", and the outcome indicated a highly effective encryption (Fig. 6d). During decryption, the encrypted matrix information was combined with the two key matrices to obtain the decryption matrix. By comparing the decryption matrix with the original data, it could be proven that the entire encryption and decryption process was effective and complete. Depending on the requirements of the actual application, the encryption level can be improved by increasing the number of keys of the encryption circuit (increasing the number of input). Additionally, the logic and number of outputs can be expanded by changing the number and order of series and parallel connections of the memristor logic gates. Based on this encryption method, binary digit groups and images can be encrypted and decrypted in a similar manner (Fig. S9).

Magnetic resonance imaging (MRI) and computed tomography (CT) images are commonly used as medical imaging modalities for diagnosis. In this work, CT images of the abdomen were used as an example. The information in these medical images was represented by gray values, which ranged between 256 levels (from 0 to 255). It is noteworthy that 256 can also be represented by an 8-bit binary array, which enables the unification in the format of medical information (texts and images). This implies that medical images can be encrypted using the same encryption rules as information of letters and numbers. In particular, the gray value information of a medical image can be represented by eight slicing matrices, with each pixel jointly represented by the same position cell of the eight slicing matrices. The effectiveness and accuracy of medical image encryption and decryption could be demonstrated by the

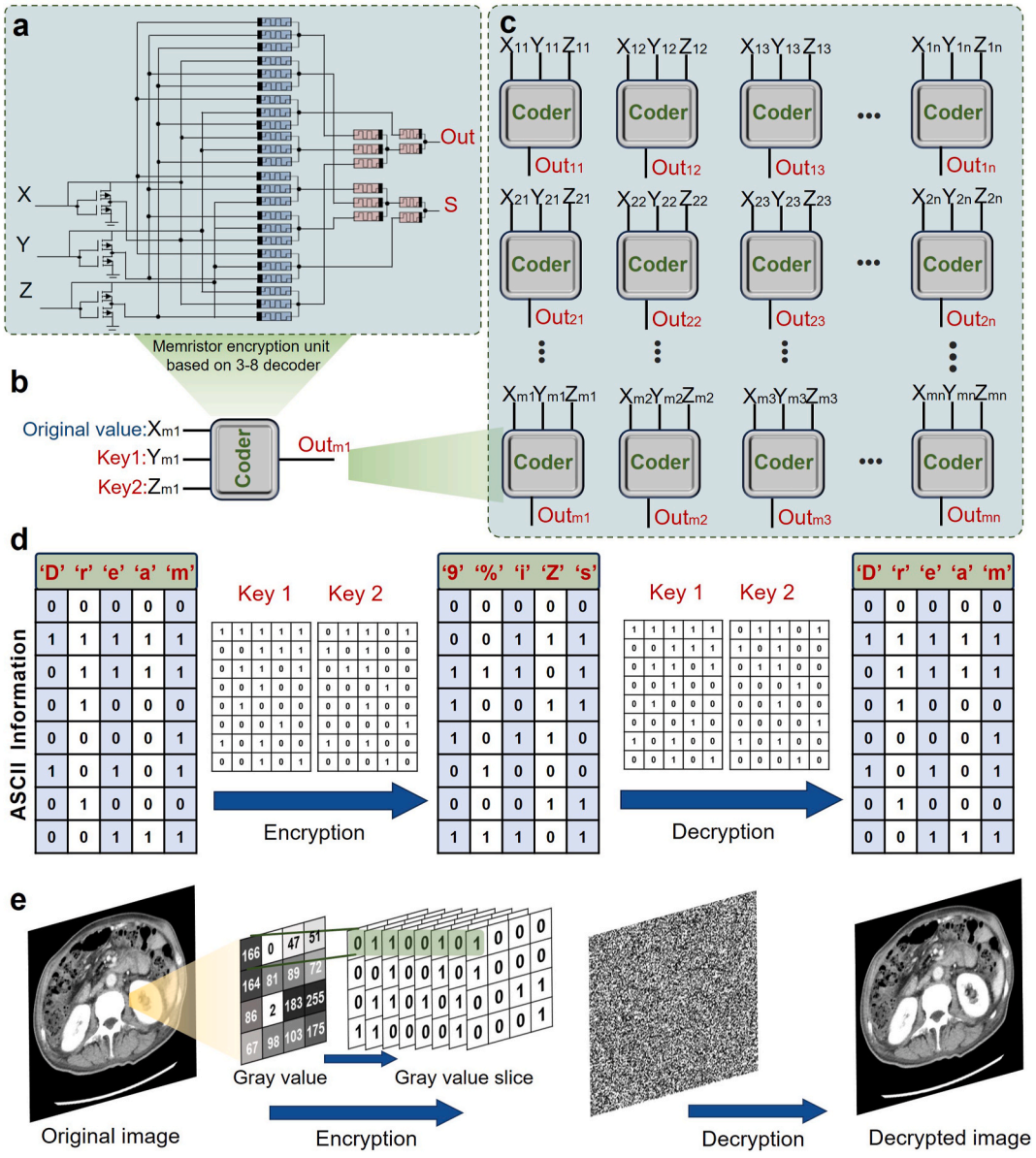

Fig. 6. (a) Memristor encryption circuit based on 3-8 decoder. (b) Encapsulation diagram of the encryption unit. (c) Encryption matrix of m × n array. (d) Encryption and decryption of medical information by ASCII. (e) Encryption and decryption of the medical image.

memristor encryption circuit based on a 3-8 decoder, which realized the unified encryption rule of medical information (Fig. 6e). Furthermore, this novel hardware encryption circuit based on biomemristors is capable of expedient and efficacious encryption and decryption of medical information, while also being environmentally friendly and cost-effective due to its utilization of natural biomaterials.

4. Conclusion

A biomemristor with Ag/mugwort: PVDF/ITO structure was prepared using spin-coating and magnetron sputtering methods. The biomemristor with the Ag/mugwort:PVDF/ITO structure exhibited excellent durability, RS behavior and unidirectional conduction properties when compared to three different top electrodes: Cu, Ti, and Ag. Furthermore, the RS behavior and unidirectional conduction properties of the biomemristor were investigated under different voltage amplitudes and scanning rates. A charge conduction model driven by a combination of F-N tunneling, redox reactions, and complexation reactions was proposed to explain the mechanisms of the memristive device. Finally, the biomemristor was used to construct novel logic gate circuits, in which a hardware-based encryption circuit was devised to realize the uniform rule encryption and decryption of medical information including data and images. This work not only shows a low-cost and environmentally friendly biomemristor, but also facilitates the integration of memristors with traditional electronic devices. These results contribute to expanding the applicability of biomemristor in digital circuits, data encryption, and medical image security.

CRediT authorship contribution statement

Fulai Lin: Writing – original draft, Methodology, Investigation, Data curation. **Yuchen Cheng:** Methodology, Formal analysis. **Zhuoqun Li:** Resources. **Chengjiang Wang:** Formal analysis. **Wei Peng:** Data curation. **Zelin Cao:** Software. **Kaikai Gao:** Software. **Yu Cui:** Validation. **Shiyang Wang:** Visualization. **Qiang Lu:** Conceptualization. **Kun Zhu:** Visualization. **Dinghui Dong:** Investigation. **Yi Lyu:** Methodology. **Bai Sun:** Writing – review & editing, Supervision, Project administration, Funding acquisition. **Fenggang Ren:** Writing – review & editing, Supervision.

Declaration of competing interest

The authors declare that they have no known competing financial interests or personal relationships that could have appeared to influence the work reported in this paper.

Data availability

Data will be made available on request.

Acknowledgements

This work was supported by the National Natural Science Foundation of China (52375575, 82200736, 52172129, 52002312), Common Technology R&D Platform of Shaanxi Province (2023GXJS-01-1-2), the Xi'an Jiaotong University for the financial support of the top young talent project (71211223010708), the Fundamental Research Funds for the Central Universities of Xi'an Jiaotong University (XZD012023065), and the Natural Science Basic Research Plan in Shaanxi Province of China (2022JQ-963).

Appendix B. Supplementary data

Supplementary data to this article can be found online at https://doi.org/10.1016/j.mtbio.2024.101257.

References

[1] K. Sun, J. Chen, X. Yan, The future of memristors: materials engineering and neural networks, Adv. Funct. Mater. 31 (2021) 2006773.
[2] X. Niu, B. Tian, Q. Zhu, B. Dkhil, C. Duan, Ferroelectric polymers for neuromorphic computing, Appl. Phys. Rev. 9 (2022) 021309.
[3] D. Gil, M. Johnsson, H. Mora, J. Szymański, Review of the complexity of managing big data of the internet of things, Complexity 2019 (2019) e4592902.
[4] S.-G. Ren, A.-W. Dong, L. Yang, Y.-B. Xue, J.-C. Li, Y.-J. Yu, H.-J. Zhou, W.-B. Zuo, Y. Li, W.-M. Cheng, X.-S. Miao, Self-Rectifying memristors for three-dimensional in-memory computing, Adv. Mater. 36 (2024) 2307218.
[5] H. Abunahla, Y. Abbas, A. Gebregiorgis, W. Waheed, B. Mohammad, S. Hamdioui, A. Alazzam, M. Rezeq, Analog monolayer SWCNTs-based memristive 2D structure for energy-efficient deep learning in spiking neural networks, Sci. Rep. 13 (2023) 21350.
[6] X. Chen, X. Zhao, X. Huang, X.-Z. Tang, Z. Sun, D.-L. Ni, H. Hu, J. Yue, Flexible multilevel nonvolatile biocompatible memristor with high durability, J. Nanobiotechnol. 21 (2023) 375.
[7] T.-K. Su, W.-K. Cheng, C.-Y. Chen, W.-C. Wang, Y.-T. Chuang, G.-H. Tan, H.-C. Lin, C.-H. Hou, C.-M. Liu, Y.-C. Chang, J.-J. Shyue, K.-C. Wu, H.-W. Lin, Room-temperature fabricated multilevel nonvolatile lead-free cesium halide memristors for reconfigurable in-memory computing, ACS Nano 16 (2022) 12979–12990.
[8] B. Yan, B. Li, X. Qiao, C.-X. Xue, M.-F. Chang, Y. Chen, H. Li, Resistive Memory-based in-memory computing: from device and large-scale integration system perspectives, Adv. Intell. Syst. 1 (2019) 1900068.
[9] J. Xiong, R. Yang, J. Shaibo, H.-M. Huang, H.-K. He, W. Zhou, X. Guo, Bienenstock, cooper, and munro learning rules realized in second-order memristors with tunable forgetting rate, Adv. Funct. Mater. 29 (2019) 1807316.
[10] S.S. Kundale, G.U. Kamble, P.P. Patil, S.L. Patil, K.A. Rokade, A.C. Khot, K. A. Nirmal, R.K. Kamat, K.H. Kim, H.-M. An, T.D. Dongale, T.G. Kim, Review of electrochemically synthesized resistive switching devices: memory storage, neuromorphic computing, and sensing applications, Nanomaterials 13 (2023) 1879.
[11] G. Zhou, Z. Wang, B. Sun, F. Zhou, L. Sun, H. Zhao, X. Hu, X. Peng, J. Yan, H. Wang, W. Wang, J. Li, B. Yan, D. Kuang, Y. Wang, L. Wang, S. Duan, Volatile and nonvolatile memristive devices for neuromorphic computing, Adv. Electron. Mater. 8 (2022) 2101127.
[12] K.-H. Kim, S. Gaba, D. Wheeler, J.M. Cruz-Albrecht, T. Hussain, N. Srinivasa, W. Lu, A functional hybrid memristor crossbar-array/CMOS system for data storage and neuromorphic applications, Nano Lett. 12 (2012) 389–395.
[13] J. Borghetti, G.S. Snider, P.J. Kuekes, J.J. Yang, D.R. Stewart, R.S. Williams, 'Memristive' switches enable 'stateful' logic operations via material implication, Nature 464 (2010) 873–876.
[14] M. Rao, H. Tang, J. Wu, W. Song, M. Zhang, W. Yin, Y. Zhuo, F. Kiani, B. Chen, X. Jiang, H. Liu, H.-Y. Chen, R. Midya, F. Ye, H. Jiang, Z. Wang, M. Wu, M. Hu, H. Wang, Q. Xia, N. Ge, J. Li, J.J. Yang, Thousands of conductance levels in memristors integrated on CMOS, Nature 615 (2023) 823–829.
[15] L. Li, D. Yu, Y. Wei, Y. Sun, J. Zhao, Z. Zhou, J. Yang, Z. Zhang, X. Yan, A $SmNiO_3$ memristor with artificial synapse function properties and the implementation of boolean logic circuits, Nanoscale 15 (2023) 7105–7114.
[16] P. Kumar, K. Zhu, X. Gao, S.-D. Wang, M. Lanza, C.S. Thakur, Hybrid architecture based on two-dimensional memristor crossbar array and CMOS integrated circuit for edge computing, Npj 2D Mater. Appl. 6 (2022) 1–10.
[17] S. Zhu, L. Wang, S. Duan, Memristive pulse coupled neural network with applications in medical image processing, Neurocomputing 227 (2017) 149–157.
[18] D. Jiang, N. Tsafack, W. Boulila, J. Ahmad, J.J. Barba-Franco, ASB-CS: adaptive sparse basis compressive sensing model and its application to medical image encryption, Expert Syst. Appl. 236 (2024) 121378.
[19] L. Minati, L.V. Gambuzza, W.J. Thio, J.C. Sprott, M. Frasca, A chaotic circuit based on a physical memristor, Chaos, Solit. Fractals 138 (2020) 109990.
[20] H. Lin, C. Wang, L. Cui, Y. Sun, C. Xu, F. Yu, Brain-like initial-boosted hyperchaos and application in biomedical image encryption, IEEE Trans. Ind. Inf. 18 (2022) 8839–8850.
[21] Y. Lu, M. Gong, Z. Gan, X. Chai, L. Cao, B. Wang, Exploiting one-dimensional improved Chebyshev chaotic system and partitioned diffusion based on the divide-and-conquer principle for 3D medical model encryption, Chaos, Solit. Fractals 171 (2023) 113449.
[22] A.F. Choudhri, A.R. Chatterjee, R. Javan, M.G. Radvany, G. Shih, Security issues for mobile medical imaging: a primer, Radiographics 35 (2015) 1814–1824.
[23] C. Yang, B. Sun, G. Zhou, T. Guo, C. Ke, Y. Chen, J. Shao, Y. Zhao, H. Wang, Photoelectric memristor-based machine vision for artificial intelligence applications, ACS Mater. Lett. 5 (2023) 504–526.
[24] G.U. Kamble, A.P. Patil, R.K. Kamat, J.H. Kim, T.D. Dongale, Promising materials and synthesis methods for resistive switching memory devices: a status review, ACS Appl. Electron. Mater. 5 (2023) 2454–2481.
[25] J. Xia, Z. Zhang, H. He, Y. Xu, D. Dong, R. Yang, X. Miao, Environment-friendly regenerated cellulose based flexible memristive device, Appl. Phys. Lett. 119 (2021) 201904.
[26] G. Zhou, Z. Ren, L. Wang, B. Sun, S. Duan, Q. Song, Artificial and wearable albumen protein memristor arrays with integrated memory logic gate functionality, Mater. Horiz. 6 (2019) 1877–1882.
[27] A. Chanthbouala, V. Garcia, R.O. Cherifi, K. Bouzehouane, S. Fusil, X. Moya, S. Xavier, H. Yamada, C. Deranlot, N.D. Mathur, M. Bibes, A. Barthélémy, J. Grollier, A ferroelectric memristor, Nat. Mater. 11 (2012) 860–864.

[28] S.N. Campelo, E.J. th Jacobs, K.N. Aycock, R.V. Davalos, Real-time temperature rise estimation during irreversible electroporation treatment through state-space modeling, Bioeng. Basel 9 (2022) 499.
[29] J. Bian, Z. Liu, Y. Tao, Z. Wang, X. Zhao, Y. Lin, H. Xu, Y. Liu, Advances in memristor based artificial neuron fabrication-materials, models, and applications, Int. J. Extrem. Manuf. 6 (2023) 012002.
[30] Y. Xiao, B. Jiang, Z. Zhang, S. Ke, Y. Jin, X. Wen, C. Ye, A review of memristor: material and structure design, device performance, applications and prospects, Sci. Technol. Adv. Mater. 24 (2023) 2162323.
[31] H. Hao, L. Yan, M. Wang, Y. Cao, J. He, Y. Yang, Research process of carbon dots in memristors, Adv. Electron. Mater. 9 (2023) 2201195.
[32] U. Celano, K. Nagashima, H. Koga, M. Nogi, F. Zhuge, G. Meng, Y. He, J. De Boeck, M. Jurczak, W. Vandervorst, T. Yanagida, All-nanocellulose nonvolatile resistive memory, NPG Asia Mater. 8 (2016) e310, e310.
[33] M.K. Hota, M.K. Bera, B. Kundu, S.C. Kundu, C.K. Maiti, A natural silk fibroin protein-based transparent bio-memristor, Adv. Funct. Mater. 22 (2012) 4493–4499.
[34] A. Han, L. Zhang, M. Zhang, C. Liu, R. Wu, Y. Wei, R. Dan, X. Chen, E. Hu, Y. Zhang, Y. Tong, L. Liu, Amyloid–gold nanoparticle hybrids for biocompatible memristive devices, Materials 16 (2023) 1884.
[35] Y. Diao, F. Yang, Y. Jia, M. Su, J. Hu, J. Sun, D. Jiang, D. Wang, Y. Pu, Y. Zhao, B. Sun, Transmission mechanism and logical operation of graphene-doped poly (vinyl alcohol) composite-based memristor, ACS Appl. Mater. Interfaces 16 (2024) 2477–2488.
[36] B. Sun, Y. Chen, G. Zhou, Y. Zhou, T. Guo, S. Zhu, S. Mao, Y. Zhao, J. Shao, Y. Li, A flexible corn starch-based biomaterial device integrated with capacitive-coupled memristive memory, mechanical stress sensing, synapse, and logic operation functions, Adv. Electron. Mater. 9 (2023) 2201017.
[37] W.S. Choi, M.S. Song, H. Kim, D.H. Kim, Conduction mechanism analysis of abrupt- and gradual-switching InGaZnO memristors, Micromachines 13 (2022) 1870.
[38] D.H. Shin, H. Park, N. Ghenzi, Y.R. Kim, S. Cheong, S.K. Shim, S. Yim, T.W. Park, H. Song, J.K. Lee, B.S. Kim, T. Park, C.S. Hwang, Multiphase reset induced reliable dual-mode resistance switching of the Ta/HfO_2/RuO_2 memristor, ACS Appl. Mater. Interfaces 16 (2024) 16462–16473.
[39] J.T. Jang, J. Min, Y. Hwang, S.-J. Choi, D.M. Kim, H. Kim, D.H. Kim, Digital and analog switching characteristics of InGaZnO memristor depending on top electrode material for neuromorphic system, IEEE Access 8 (2020) 192304–192311.
[40] Y. Park, J.-S. Lee, Artificial synapses with short- and long-term memory for spiking neural networks based on renewable materials, ACS Nano 11 (2017) 8962–8969.
[41] A.R. Patil, T.D. Dongale, L.D. Namade, S.V. Mohite, Y. Kim, S.S. Sutar, R.K. Kamat, K.Y. Rajpure, Sprayed $FeWO_4$ thin film-based memristive device with negative differential resistance effect for non-volatile memory and synaptic learning applications, J. Colloid Interface Sci. 642 (2023) 540–553.
[42] S. Fatima, X. Bin, M.A. Mohammad, D. Akinwande, S. Rizwan, Graphene and MXene based free-standing carbon memristors for flexible 2D memory applications, Adv. Electron. Mater. 8 (2022) 2100549.
[43] X. Shan, P. Liu, F. Wang, Y. Xie, J. Wei, Z. Ma, Y. Shi, H. Sun, S. Lu, Z. Song, X. Yan, K. Zhang, Dual-conductivity mechanism investigation of 2D α-MoO_3-based multi-level memristor, Sci. China Mater. 66 (2023) 4773–4781.
[44] H. Liang, C. Ke, B. Sun, S. Zhu, Q. Wen, M. Huang, J. Wang, Y. Zhao, Stable resistive switching behavior of polyvinyl alcohol coating film-based memristor under multiple operating voltages by doping AgNWs, Colloids Surf. A Physicochem. Eng. Asp. 675 (2023) 132053.
[45] Y. Wang, G. Zhou, B. Sun, W. Wang, J. Li, S. Duan, Q. Song, Ag/HfOx/Pt unipolar memristor for high-efficiency logic operation, J. Phys. Chem. Lett. 13 (2022) 8019–8025.
[46] W. Wang, G. Zhou, Y. Wang, B. Yan, B. Sun, S. Duan, Q. Song, Multiphotoconductance levels of the organic semiconductor of polyimide-based memristor induced by interface charges, J. Phys. Chem. Lett. 13 (2022) 9941–9949.
[47] M.K. Hota, M.K. Bera, B. Kundu, S.C. Kundu, C.K. Maiti, A natural silk fibroin protein-based transparent bio-memristor, Adv. Funct. Mater. 22 (2012) 4493–4499.
[48] D. Li, C. Li, J. Wang, M. Xu, J. Ma, D. Gu, F. Liu, Y. Jiang, W. Li, Multifunctional analog resistance switching of Si_3N_4-based memristors through migration of Ag^+ ions and formation of Si-dangling bonds, J. Phys. Chem. Lett. 13 (2022) 5101–5108.
[49] S. Mao, Z. Cao, X. Zheng, G. Zhou, J. Qin, Y. Yang, M. Liu, Z. Rao, Y. Zhao, B. Sun, Multi-factors-regulated multi-level down-scalable and robust memristors, Mater. Today Chem. 35 (2024) 101876.
[50] S. Kim, S. Jung, M.-H. Kim, Y.-C. Chen, Y.-F. Chang, K.-C. Ryoo, S. Cho, J.-H. Lee, B.-G. Park, Scaling effect on silicon nitride memristor with highly doped Si substrate, Small 14 (2018) 1704062.
[51] J. Wang, H. Wang, Z. Cao, S. Zhu, J. Du, C. Yang, C. Ke, Y. Zhao, B. Sun, Logic gate circuits based on CeO_x/WO_y memristor for the odd/even checker and encryption/decryption of image applications, Adv. Funct. Mater. 34 (2024) 2313219.
[52] K. Zhang, Q. Xue, C. Zhou, W. Mo, C.-C. Chen, M. Li, T. Hang, Biopolymer based artificial synapses enable linear conductance tuning and low-power for neuromorphic computing, Nanoscale 14 (2022) 12898–12908.
[53] N. Padma, C.A. Betty, S. Samanta, A. Nigam, Tunable switching characteristics of low operating voltage organic bistable memory devices based on gold nanoparticles and copper phthalocyanine thin films, J. Phys. Chem. C 121 (2017) 5768–5778.
[54] Y. Nishidono, T. Chiyomatsu, K. Sanuki, Y. Tezuka, K. Tanaka, Analysis of seasonal variations of the volatile constituents in artemisia princeps (Japanese mugwort) leaves by metabolomic approach, Nat. Prod. Commun. 14 (2019) 1934578X19872600.
[55] E. Pannacci, M. Masi, M. Farneselli, F. Tei, Evaluation of mugwort (Artemisia vulgaris L.) aqueous extract as a potential bioherbicide to control amaranthus retroflexus L. in maize, Agriculture 10 (2020) 642.
[56] R.M.A. Oliveira, J.D.O. Henriques, A. Sartoratto, M.R.W. Maciel, P.F.M. Martinez, Evaluation of limonene in sugarcane wax extraction, Sustain. Chem. Pharm. 27 (2022) 100657.
[57] A. Pena, S. Veiga, M. Sapelli, N. Martínez, V. Márquez, E. Dellacassa, J. Bussi, Limonene oxidation by molecular oxygen under solvent-free conditions: the influence of peroxides and catalysts on the reaction rate, React. Kinet. Mech. Catal. 107 (2012) 263–275.
[58] N.N. Mobarak, F.N. Jumaah, M.A. Ghani, M.P. Abdullah, A. Ahmad, Carboxymethyl carrageenan based biopolymer electrolytes, Electrochim. Acta 175 (2015) 224–231.
[59] M.-K. Kim, J.-S. Lee, Short-term plasticity and long-term potentiation in artificial biosynapses with diffusive dynamics, ACS Nano 12 (2018) 1680–1687.
[60] X. Wang, Y. Sun, J. Zhou, X. Chen, S.-M. Kang, H.H.-C. Iu, Design method for unbalanced ternary logic family based on binary memristors, Nonlinear Dynam. 112 (2024) 7615–7629.
[61] M.-K. Song, J.-H. Kang, X. Zhang, W. Ji, A. Ascoli, I. Messaris, A.S. Demirkol, B. Dong, S. Aggarwal, W. Wan, S.-M. Hong, S.G. Cardwell, I. Boybat, J. Seo, J.-S. Lee, M. Lanza, H. Yeon, M. Onen, J. Li, B. Yildiz, J.A. del Alamo, S. Kim, S. Choi, G. Milano, C. Ricciardi, L. Alff, Y. Chai, Z. Wang, H. Bhaskaran, M.C. Hersam, D. Strukov, H.-S.P. Wong, I. Valov, B. Gao, H. Wu, R. Tetzlaff, A. Sebastian, W. Lu, L. Chua, J.J. Yang, J. Kim, Recent advances and future prospects for memristive materials, devices, and systems, ACS Nano 17 (2023) 11994–12039.
[62] Y. Ding, F. Tan, Z. Qin, M. Cao, K.-K.R. Choo, Z. Qin, DeepKeyGen: a deep learning-based stream cipher generator for medical image encryption and decryption, IEEE Transact. Neural Networks Learn. Syst. 33 (2022) 4915–4929.
[63] Y. Wu, L. Zhang, S. Berretti, S. Wan, Medical image encryption by content-aware DNA computing for secure healthcare, IEEE Trans. Ind. Inf. 19 (2023) 2089–2098.